Provenance of Tibetan Geoid Ridge and its Implication to the Collision Evolution between India and Tibet

Peilong Yan[1], Nan Zhang[*1], Xi Liu[2], Bo Wan[3]

[1] The Key Laboratory of Orogenic Belts and Crustal Evolution, School of Earth and Space Sciences, Peking University, Beijing 100871, China

[2]Center of Deep-Sea Research, Institute of Oceanology, Chinese Academy of Sciences, Qingdao 266071, China

[3]State Key Laboratory of Lithospheric Evolution, Institute of Geology and Geophysics, Chinese Academy of Sciences, Beijing 100029, China

*Corresponding Author: Nan Zhang (nan_zhang@pku.edu.cn)

Submitted to *Geophysical Research Letters*

Key Points:

- Tibetan Geoid Ridge is mainly contributed by degrees 7 to 10 and it is caused by the mantle transition zone density structure.
- Geoid calculation supports a high-density structure in the mantle transition zone beneath the Tibetan Plateau.
- Geoid calculation suggests the Indian slab subduction is more possible than the lithospheric dripping in the Tibetan Plateau evolution.

Abstract

The geoid minima in the Indian Ocean and North Eurasia are separated by the Tibetan Geoid Ridge (TGR), yet the origin of TGR remains poorly constrained. Spherical harmonic analysis and geoid kernels indicate that the TGR has wavelengths of degrees 7-10 and is generated by density anomalies of degrees 7-10 in the mantle. By employing numerical geoid modelling with four different tomography-derived density structures, we determined that abundant high-density anomalies in the mantle transition zone beneath Tibet are responsible for TGR. Additionally, two previously proposed alternative evolving scenarios of the India-Tibet collision — Indian lithosphere subduction and Tibetan lithosphere dripping — are evaluated through geoid calculation. The former suggests abundant high-density structures in the Tibetan transition zone, which can generate a well-constrained TGR, while the latter does not. Therefore, we regard the Indian lithosphere subduction as a more plausible evolving scenario.

Plain Language Summary

Density anomalies in the Earth's interior affect the Earth's gravitational potential field. Satellite gravity surveys reveal a gravitational potential anomaly in Tibet, referred to as the Tibetan Geoid Ridge (TGR). We utilize spectrum analysis to determine the size of TGR and its density source, and three-dimensional (3D) modeling to predict the Tibetan gravitational potential field and determine the density source of the TGR. In the 3D modelling, we test different density anomaly distribution models acquired from seismic waves. By evaluating the correlation between the calculated results of different models and observations, we ascertain that the abundant high-density materials beneath Tibet, from 410 km to 660 km in depth, can generate the best-fit TGR and could be the source of the TGR. Additionally, the modeling provides constraints on the

geological evolution of Tibet. Two alternative Tibetan evolution scenarios have been proposed previously: one suggests that the Indian lithosphere subducts into the mantle, and the other suggests that the Tibetan lithosphere drips into the mantle. The former scenario is consistent with the existence of the abundant high-density structures mentioned before, which can generate TGR well, but the latter scenario cannot. Therefore, our modeling supports the Indian lithosphere subduction scenario.

1 Introduction

The global geoid low features a semi-continuous geoid trough stretching longitudinally, including geoid lows in the Indian Ocean, Antarctica, Siberia, and North America (Spasojevic et al., 2010). These geoid lows are separated by several relatively higher, ridge-like geoid anomalies in Tibet, South Indian Ocean, and South America (Figure 1a). These geoid anomalies originate from the Earth's interior and offer critical insights into the mantle's density distribution. Recently, the origin of the geoid lows, especially the Indian Ocean Geoid Low (IOGL) has aroused many discussions (Ghosh et al. 2017, Ghosh & Pal 2022, Nerlich et al. 2016, Pal & Ghosh 2023, Spasojevic et al. 2010 and Steinberger et al. 2021). However, there has been less research (Pal & Ghosh, 2023) concerning the origin of the geoid ridges, which separate geoid lows within the trough.

Among these geoid ridges, the Tibetan Geoid Ridge (TGR) is particularly interesting, for it not only separates the large Indian Ocean and Siberian geoid minima but also coincides with the intensive continental collision region (Figure 1a). Although the Tibetan plateau has the highest topography, it is generally considered an equilibrious plateau (Jiménez-Munt et al. 2008, Ravikumar et al. 2020). How the intense continental convergence between Indian sub-continent

and Asia changes the underlying mantle structure and gravitational potential, and hence alters the long-wavelength geoid lows is a question.

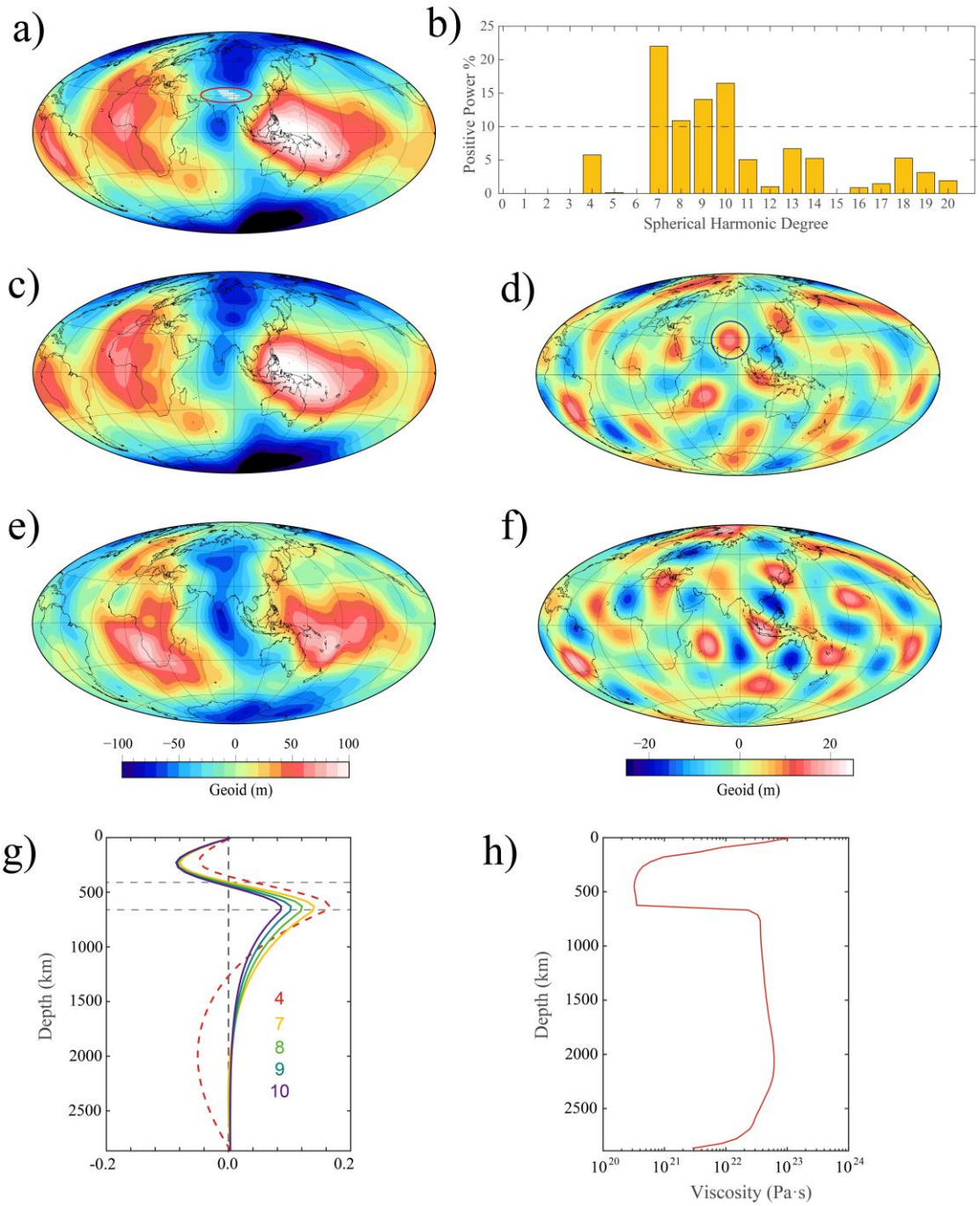

Figure 1. a). Observed geoid from Chambat et al. (2010). White area refers to the TGR sample points. b). The positive contribution to the TGR from different wavelengths. c). Geoid observation without degrees 7-10. d). Degrees 7-10 components of the geoid observation. e). Calculated geoid

using tomography model GYPSUM-S. f). Degrees 7-10 components of GYPSUM-S calculated geoid. g). Geoid kernel calculated from the earth's 1D viscosity profile shown in h).

Specifically, we seek the mantle density source of the TGR. We first examine the wavelength of the observed TGR by spherical harmonic expansion. By doing this, we constrain the wavelength of the density source responsible for the TGR. Then, we calculate the geoid kernel associated with an Earth's representative 1D viscosity profile (Liu & Zhong, 2015). Analyzing the kernel, we further narrow down the depth range of the density source. Additionally, we employ instantaneous geoid modelling driven by the tomography-derived density structures. These structures either suggest a large amount of denser materials or only small-scale dense materials in the Tibetan transition zone. Comparing the geoid patterns generated by these different density structures with the observed geoid, we suggest a large-scale dense Tibetan transition zone as a more likely structure, for it can account for the generation of the TGR. These dense materials in the Tibetan transition zone are interpreted as subduction remnants. This result prefers the Indian slab subduction, rather than the Tibetan lithosphere dripping as the evolution scenario of the India-Tibet convergence.

2 Methods and Materials

2.1 Spherical Harmonic Wavelength and Geoid Kernel Analysis

To delimit the size (wavelengths) and depths of mantle density anomalies that contribute predominantly to the TGR, two steps are employed: (1). Decompose the spherical harmonic components of the observed regional geoid data, which can determine the TGR's dominant

wavelengths. (2). Calculate and analyze the geoid kernel, which can connect the prominent geoid wavelengths of TGR to the corresponding depth ranges and wavelengths of the mantle density. For the former step, we first select the observed geoid data points in a region that covers the TGR by the grid of 2°×2° as the sample points (white area in Figure 1a). This region (red circle in Figure 1a) is sandwiched between the IOGL and the Siberian Geoid Low. It spans 300 km along the Tibetan Plateau near the latitude of 30°N. All of these sample points are above -35 m and represent the TGR here. Then, we conduct spherical harmonic expansion to the observed geoid data (Figure 1a). For these sample points:

$$h(\theta,\phi)=\sum_{l=2}^{20}\sum_{m=0}^{l}[a_{lm}cos(m\phi)+b_{lm}sin(m\phi)]p_{lm}(\theta,\phi),$$

where θ, Φ are colatitude and longitude of the sample point, h is the geoid height of the sample point, l is the spherical harmonic degree expanded up to degree 20, m is the spherical harmonic order, a_{lm} is the cosine term of the spherical harmonic coefficient while b_{lm} is the sine term, and p_{lm} is a normalized associated Legendre polynomial. To analyze the geoid contribution of every single-degree component to the TGR, we averaged the single-degree geoid value of these sample points. Because the spatial sampling density depends on the latitude (proportional to $sin\theta$), we weight every sample point with $sin\theta$ when calculating the average. Then, the averaged geoid value in degree l is:

$$\bar{h}_l=\frac{\sum_{i=1}^{N}h_l(\theta_i,\phi_i)sin\theta_i}{N}=\frac{\sum_{i=1}^{N}\sum_{m=0}^{l}[a_{lm}cos(m\phi_i)+b_{lm}sin(m\phi_i)]p_{lm}(\theta_i,\phi_i)sin\theta_i}{N},$$

where θ_i, Φ_i are the coordinates of the sample point i, N is the number of sample points. Since TGR is a relatively geoid higher region, we focus on the positive contribution to TGR and neglect all of the negative contributed degrees. We get the proportion of single-degree positive

contribution as:

$$P_{l_0} = \frac{\bar{h}_{l_0}\delta}{\sum_{l=2}^{20}(\bar{h}_l\delta)} \times 100\%,\ \delta = \begin{cases} 0, & \bar{h}_l \leq 0 \\ 1, & \bar{h}_l > 0 \end{cases}$$

Comparing P_l of every degree, the dominant wavelengths of the TGR can be determined.

The dominant geoid wavelengths are controlled by the same wavelengths of density anomaly at varying depths (Zhong et al., 2008). For each degree, the geoid can be expressed by multiplying the expansion coefficients of density at each depth, by a depth-dependent geoid kernel (Richards and Hager, 1984; Ricard et al., 1984). The geoid kernel value can be positive or negative, it represents a unit of high-density anomaly generates a higher or lower geoid anomaly (Richards and Hager, 1984). With a radial viscosity structure (like Figure 1h), the geoid kernel also can be obtained analytically through a propagator matrix method (Hager and O'Connell, 1979, 1981).

2.2 Numerical Geoid Modeling

After constraining the wavelengths of the TGR's density origin, we further examine the geoid contribution of density structures at various depth ranges. We employ seismic tomography models as the three-dimensional mantle density structure and calculate the global geoid by solving the Stokes flow numerically. We use the three-dimensional viscous finite element convection code CitcomS (Zhong et al., 2008) to calculate gravitational potential from mantle flow. Our calculations are based on the governing equations for mass and momentum conservation, assuming an incompressible fluid (Liu & Zhong, 2016; Mao & Zhong, 2019, 2021). The model has 65×65×65 nodes with an average horizontal grid size of 1°×1°. Seismic velocity anomalies

(see Section 2.3) are converted into density anomalies, which drive the mantle flow. Based on the previous test of the affection of velocity-density conversion (Ghosh et al., 2010, 2017), we maintain a constant velocity-density scaling ($dln\rho/dlnV_S$) of 0.25 for the S wave model throughout the mantle. The geoid is calculated up to degree 20, accounting for the effects of self-gravitation. Geoid responses of the surface and core-mantle boundary topographies are also considered (Adam et al., 2014; Hager, 1984). Computed geoid is compared with the observed geoid data from Chambat et al. (2010), which is referenced to the hydrostatic equilibrate Earth.

Both radial and lateral viscosity variations are included in the geoid calculation. We follow the methodology adopted by Ghosh et al. (2010) and Liu & Zhong (2015). The radial and lateral variations are added by introducing temperature-dependent viscosity with a depth-dependent viscosity pre-factor. Viscosity varies with temperature and depth as

$$\eta(r,T) = \eta_0(r) \cdot e^{E\cdot(T_0-T)}$$

$\eta_0(r)$ is depth-dependent viscosity pre-factor. We use a three-layer radial viscosity structure divided into lithosphere (0–100 km, η_0=0.1), upper mantle (100–660 km, η_0=0.0333), and lower mantle (660 km-CMB, η_0=3.3333). T_0 and T are the non-dimensionalized reference and actual temperatures and T_0 is set as 0.5. E, fixed as 9.2103, is the activation energy and gives an up to 10^3 viscosity contrast. Thermal expansivity is set as 3×10^{-5} K^{-1} to convert residual temperature to density anomalies. Temperature is non-dimensionalized by dividing with a scaling of 1300 K. Horizontal averaged 1D viscosity profile is shown in Figure 1h. Models are calculated with free slip boundary conditions both at the surface and the core-mantle boundary.

2.3 Examining Seismic Tomography Models

We employ four different S-wave seismic tomography models: GYPSUM-S (Simmons et al., 2010a), SEMUCB-WM1 (French & Romanowicz, 2014a), SL2013sv (Schaeffer & Lebedev, 2013a), and EARA2014 (Chen et al., 2015) as mantle density structures in geoid modelling. Previous studies (Ghosh et al., 2017, 2022) reveal the global, whole-mantle tomography model GYPSUM-S can generate a global geoid with the highest correlation to the global geoid observation (correlation coefficient = 0.90, Figure S1), although the Tibetan geoid pattern does not match the observation well. To optimize the correlation in the Tibetan region, three alternative models are introduced. The SEMUCB-WM1 model, another global whole-mantle tomography model, can generate a higher geoid field in the Tibetan region than other global tomography models (Ghosh et al. 2022, Figure S1). Another two regional models are included: SL2013sv focuses on the morphology of the subducted slab under the Tethyan region with about 280 km resolution (van der Meer et al., 2018) and EARA2014 with a fine resolution of 120 km specifically focuses on the Asian, especially Tibetan lithosphere. These two regional models support two end-members of India-Tibet convergence evolution. The former suggests a subduction-induced dense slab structure between 410 and 660 km (van der Meer & van Hinsbergen, 2018), while the latter suggests a drip-induced dense lithospheric root in the asthenosphere (Chen et al., 2017). Besides examining the geoid signals from individual tomography models, we also insert regional tomography structures from SEMUCB-WM1, SL2013sv, and EARA2014 into the GYPSUM-S model to fit in both the global and TGR geoid and finally sort out the best regional mantle structures for producing the TGR. This signal analysis based on mantle structure combinations has been used in previous studies (Ghosh et al., 2010,

Steinberger et al., 2021).

3 Results

Firstly, spherical harmonic analysis decomposes the dominant wavelengths of the TGR. As depicted in Figure 1b, degrees 7 to 10 components contribute substantially to the positive anomalies in the Tibet region: P_7, P_8, P_9, and P_{10} each account for over 10% individually and when combined, they constitute more than 60% in total. Figure 1c presents the observed geoid with degrees 7 to 10 removed. Compared with the unfiltered geoid (Figure 1a), the geoid values in the northern India and Tibetan region are notably reduced. Consequently, the TGR is weakened, and the IOGL even connects with the Siberian Geoid Low (Figure 1c). Figure 1d illustrates the degrees 7 to 10 components of the observed geoid. This wavelength range gives a significant uplift (over 20 m) to the geoid in northern India and Tibet. Based on these results, we determine that the TGR mainly features degrees 7 to 10 wavelengths.

Then, analyzing the calculated geoid kernel (Figure 1g), we linked the TGR's wavelength with the depth of its density source. As the geoid kernels show (Figure 1g), the degrees 7 to 10 kernels are negative in the upper mantle and lithosphere, so negative density anomalies in degrees 7 to 10 enhance the geoid high in the same wavelengths. However, they turn positive at about 410 ~ 440 km (from degree 7 to degree 10). So, below these depths, positive density anomalies enhance the geoid high in these wavelengths (including the Tibetan geoid high shown in Figure 1d). As they go deeper, they rise steeply in the transition zone and up to a peak at about 660 km. Then, they decrease slowly in the lower mantle.

To constrain the depth range of the density source of TGR, we calculate the global geoid numerically by employing the GYPSUM-S tomography model as the mantle density structure. Figure 1e shows our predicted geoid based on the GYPSUM-S model, which is similar to Ghosh et al. (2022) (top right panel in Figure S1). Figure 1f shows the degrees 7-10 components of Figure 1e. To figure out the geoid response of different density depth ranges individually, we divide the mantle into 150-410 km (upper mantle), 410-660 km (transition zone), and 660-1000 km (lower mantle). Depths below 1000 km are not included, because the degrees 7-10 geoid kernels are too small to consider. Degree 7-10 density anomalies in these three depth ranges are further eliminated or remain in geoid calculation. In Figure S2b, d, and f are predicted geoids without the degree 7-10 density structure in 150-410 km, 410-660 km, and 660-1000 km respectively, and c, e, and g are geoids derived only by degree 7-10 density anomalies in these depth ranges. These calculated results indicate the structure in the transition zone (410-660 km, Figures S2d and e) generates a far more pronounced Tibetan geoid high, compared with other parts (Figures S2b, c, f, and g). Here, the predominant wavelengths (degrees 7-10) and depth ranges (410-660 km) that contribute to the TGR are determined.

However, the location, intensity, and morphology of the density origin of TGR are still undetermined. We capture them by trying different tomography-derived density structures under Tibet, which are used as individual inputs to calculate the geoid and evaluate its correlation with the observed geoid. Although the whole-mantle global tomography model GYPSUM-S predicts the best global geoid (Figure 1e, Ghosh & Pal, 2022; Comparison in Figure S1), the predicted

geoid in the TGR region (Figure 1a) is much lower than the observation. Focusing on the specific wavelengths of Tibetan geoid high (i.e., sum of degrees 7-10), the signal from the GYPSUM-S prediction (Figure 1f) is fairly obscure than the observation (Figure 1d). To optimize this misfit, we explore other global tomography models. According to the results from Ghosh et al. (2022), except for two very low global amplitude models DETOXP2 and DETOXP3 (bottom panels in Figure S1c), all other models generate geoid values at the TGR region lower than the observation (Figure S1c). Among all these tomography-derived geoids, the SEMUCB-WM1 shows the highest geoid in the TGR region (Figure S1b vs. Figure 1f), although the shapes of IOGL and Siberia geoid low do not fit well (Figure S1a and left middle panel in Figure S1c; Ghosh et al., 2022). To generate a global geoid which not only fits the observation globally (including IOGL and Siberia) but also has a higher geoid in the TGR region, we adjust the mantle density structure by replacing alternative regional tomography models.

This adjustment is conducted by replacing the GYPSUM-S transition zone density structure in a local region (red line in Figure 3a, 60°E to 97°E, 20°N to 40°N) with other tomographic models. The replacing depth and region of the tomographic structures are determined by the location of degrees 7-10 pattern which dominantly contributes to the Tibetan geoid maximum (Figure 1d). As we mentioned, the degrees 7-10 Tibetan geoid high is controlled by the density anomalies in the same wavelengths. Therefore, the selected replacing region (red line in Figure 3a) corresponds to the location of the degrees 7-10 Tibetan geoid maximum in Figure 1d. To verify that the TGR is mainly contributed by the degrees 7-10 structure under Tibet, rather than the same wavelength structure somewhere else, we eliminate the degrees 7-10 structure beneath Tibet, and the geoid

predicted by non-Tibetan structure cannot reproduce TGR well. Our adjustment is limited in the transition zone, for it is highly sensitive to the TGR signal.

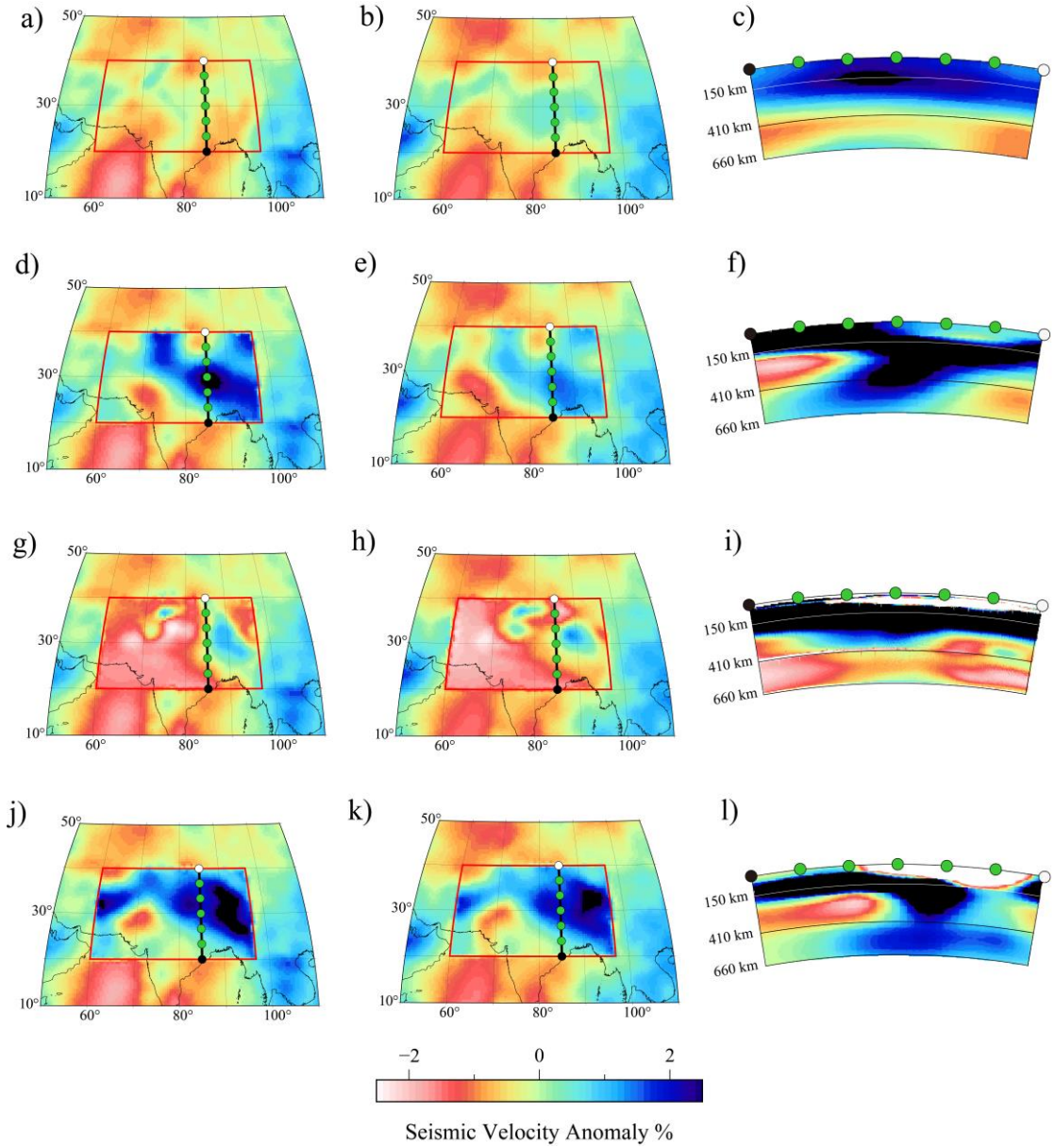

Figure 2. Seismic anomalies of GYPSUM-S: a). 462 km, b). 600 km, c). Cross-section. d-e): 462 km, 600 km of SEMUCB-WM1 (within the red line) nested in the GYPSUM-S model (outside of the red line). f): cross-section of SEMUCB-WM1 model. g-i): same as d-f) but for the EARA2014 model. j-l): same as d-f) but for the SL2013sv model.

Since the SEMUCB-WM1 model generates the TGR high the best (Section 2.3, Figure S1), we first replace the transition zone density within the selected region (Figure 2a-c; Figure 3a) of GYPSUM-S with the SEMUCB-WM1 (Figure 2d-f) to get a best-fit geoid both in the global pattern and in the TGR region. This local data replacement makes the IOGL and Siberia geoid low more isolated (Figure 3c) and enhances the TGR high. To discover which density structure produces this change, we dig into the replacing structures of these two models (Figure 3b vs. 3c). SEMUCB-WM1 shows larger and higher wave-speed (or density) anomalies (Figure 2d-f) than GYPSUM-S (Figure 2a-c) within this region. Therefore, we suggest that the SEMUCB-WM1-derived high-density anomalies in Tibetan mantle transition zone enhance the intensity of the TGR. To further confirm this, we employ two regional tomography models: EARA2014 and SL2013sv, in geoid calculation. With higher resolutions, they are well-interpreted in the Tibetan region, especially for the India-Tibet convergence. Specifically, EARA2014 suggests a lower wave-speed (light) Tibetan transition zone (Figure 2g-i) while SL2013 suggests an intense high wave-speed (dense) structure (Figure 2j-l). Consistently, calculation results show that the denser structure (SL2013; Figure 2l) generates a more salient TGR (Figure 3e) but the lighter structure (EARA2014; Figure 2i) even eliminates the TGR (Figure 3d). Comparing these three combination models, we suggest that embedding the Tibetan transition zone structures from SL2013sv within the GYPSUM-S global mantle structure can generate the best-fit geoid (Figure 3e), both on a global scale and in the TGR region. Therefore, we determine the high-density materials in the Tibetan transition zone (as the SL2013sv reveals) as the dominant mantle density origin of the TGR (Figure 4).

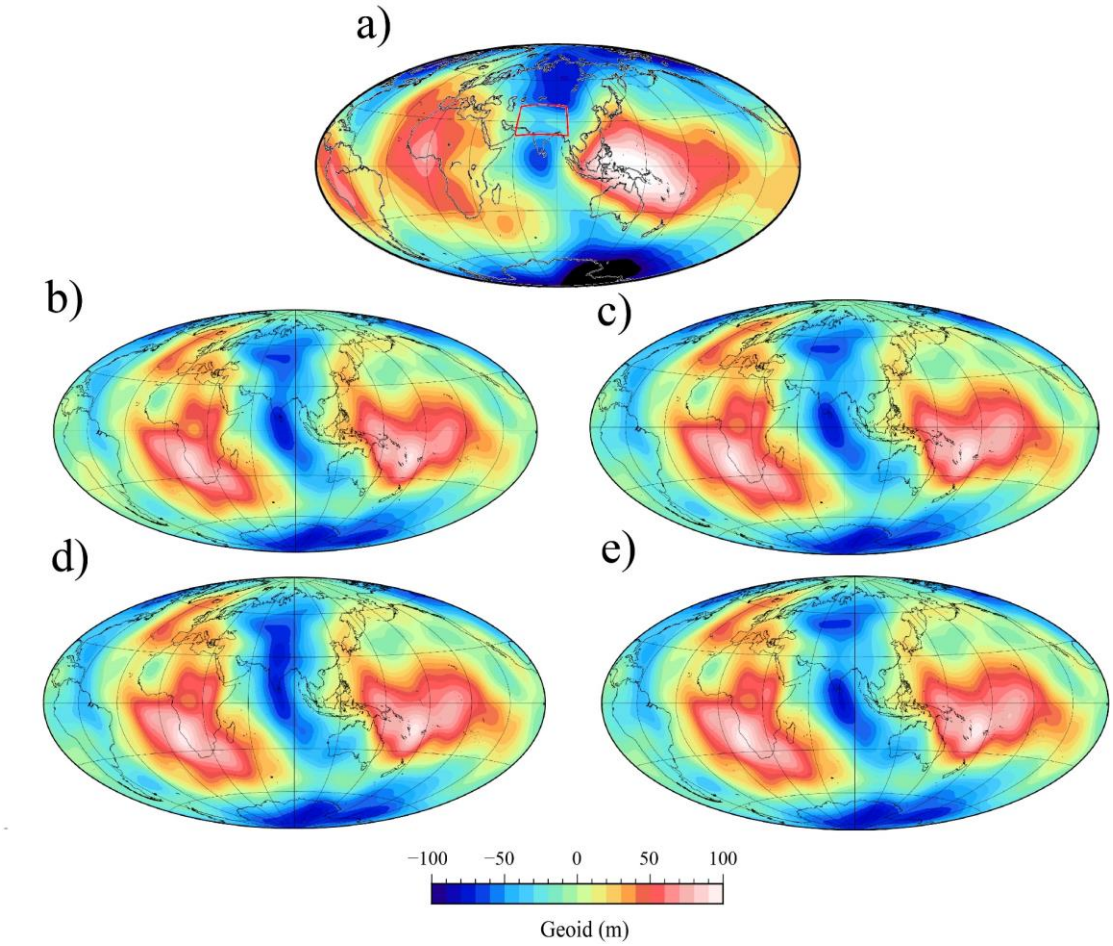

Figure 3. a). Observed geoid. Red line: model replacing region. b-c): geoid calculation results generated by b). GYPSUM-S only, c). SEMUCB-WM1 nested in GYPSUM-S, d). SL2013sv nested in GYPSUM-S, e). EARA2014 nested in GYPSUM-S.

4 Discussion

Our predicted global geoid based on GYPSUM-S and SEMUCB-WM1 reproduces the previous results (Ghosh & Pal, 2022) and fits in the observation in the first order. More importantly, with the replacement of regional tomographic structure for the global tomographic structure in the transition zone, we can produce both global and Tibetan geoid patterns (Figure 3e). Previous geoid predictions focused on IOGL (Ghosh et al., 2017; Ghosh & Pal, 2022; Pal &

Ghosh, 2023; Steinberger et al., 2021) and only occasionally produced a weak geoid ridge in Tibet (Ghosh & Pal, 2022; Pal & Ghosh, 2023), we first achieve such a good TGR through the combination of multiple tomographic models.

Although our depth sensitivity test in the result section was only based on GPYSUM-S model, the three-layer density structures from SEMUCB-WM1, SL2013sv, and EARA2014 should not affect our geoid prediction. In 150-410 km, these three models show positive density anomalies (Figure 2f, i, and l). With a negative geoid kernel at this depth (Figure 1g), these positive density anomalies produce negative geoid signals and cannot contribute to the TGR. Below 660 km, positive densities in these three models are less intense than those in GPYSUM-S, which should not produce any positive geoid stronger than GPYSUM-S. For the high-density structures in the transition zoom (Figure 2), our geoid results (Figure 3) showed consistent positive contributions from these density structures. To further investigate the role of low-density anomalies, we remove the Tibetan transition zone low-density anomalies in all four tomography models and calculate the geoid response again (shown in Figure S4 b, d, f, h). After removing the low-density anomalies, the geoid patterns based on GYPSUM-S, SEMUCB-WM1, and SL2013 models (Figure 2) change slightly. However, for the EARA2014 model, the TGR becomes more distinct (Figure S4h). This directly shows that the existence of a large number of low-density anomalies (Figures 2g, h, and i) in the Tibetan transition zone leads to an unrealistic low geoid in the TGR (Figures 3d and S4g).

The comparison between the SL2013sv and the EARA2014-derived geoids provides an independent constraint on the collision and deformation evolution of the Tibetan plateau. The

collision and deformation evolution under the Tibetan plateau has been debated between Indian subduction (van der Meer et al., 2018) and thickened lithosphere dripping (Chen et al., 2017). The debate is previously based on the interpretation of different imaged mantle structures (EARA2014 vs. SL2013sv). For the subduction model, van der Meer et al. (2018) interpret the SL2013sv's positive seismic anomalies under Tibet (Figures 2j-l and 4) as a northward subducted Greater Indian slab during 50 Ma to 15 Ma with an overturned south-dipping morphology (Figures 2l, and 4; Replumaz et al., 2010). The slab penetrates the transition zone and makes a high-velocity-dominated transition zone. Many other studies support this structure and interpretation (Hafkenscheid et al., 2006, Parson et al., 2020, Replumaz et al., 2014, van der Voo et al., 1999, van Hinsbergen et al., 2019). For the dripping model, Chen et al. (2017) interpreted the EARA2014's Tibetan structure as the dripped Tibetan lithosphere (TL). The dripped TL sinks to the transition zone, although it is too small to influence the low-velocity dominated transition zone structure. In summary, the dripping model corresponds to a small number of dense anomalies in the transition zone while the subduction model corresponds to a much denser transition zone. Many previous seismological studies attempt to constrain these two alternative scenarios (Duan et al. 2017, Li et al., 2020, Wang et al., 2019, Wu et al., 2022, Xu et al., 2020). Our geoid calculation provides a new independent constraint to these two tomography models and the evolution scenarios behind them from a gravitational perspective. Based on our geoid calculation, the SL2013sv model, which supports the subduction model, can generate a more realistic geoid than the EARA2014 model, which supports the dripping model. Therefore, we support that the Indian subduction scenario could be a more plausible evolving scenario.

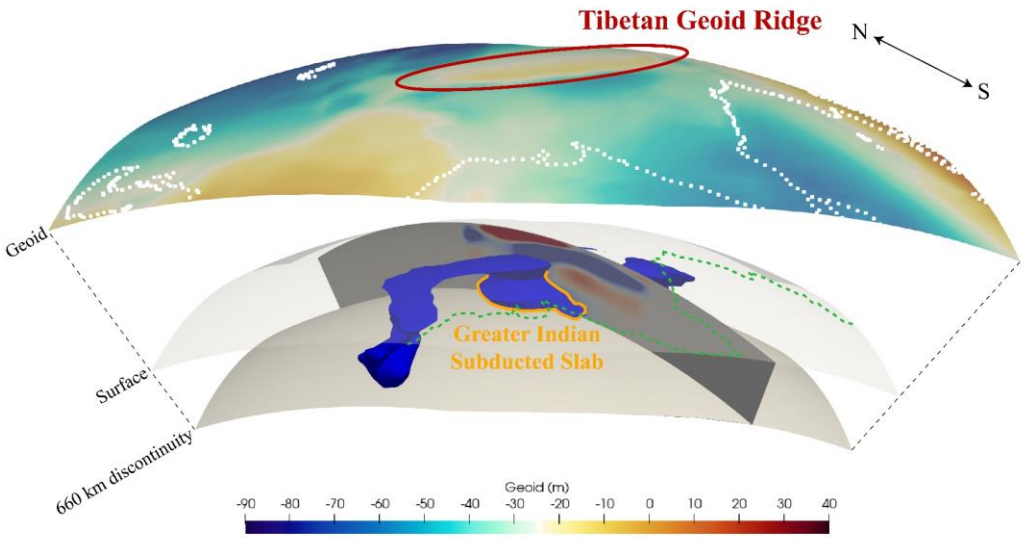

Figure 4. Location correspondence of the TGR and the tomography-predicted subducted slab. Blue bulk: Contour of the high-velocity anomaly from SL2013sv (250-660 km). The cross-section shows the shallower structure.

Figure 4 summarizes the preferred SL2013sv transition zone structure and observed Tibetan geoid. As it shows, the wide subducted slab in the transition zone is exactly vertically beneath the TGR. Based on Figure 4, we suggest the TGR generation as follows: The Greater Indian lithosphere began to subduct at 50 Ma and terminated at 15 Ma. The subducted slab kept sinking into the deep mantle after undergoing an overturn process and remains in the current mantle transition zone. The slab remnant in the transition zone has degree 7-10 wavelengths and affects the degree 7-10 components of the surface geoid. According to the geoid kernel, these density anomaly wavelengths highly contribute to the geoid positively. Therefore, at the corresponding location of the subducted slab, a relatively high geoid anomaly: Tibetan Geoid Ridge (TGR), is generated.

5 Conclusion

In this study, we determine the origin of the Tibetan Geoid Ridge by spherical harmonic analysis and global geoid calculation. Additionally, the geoid calculation also constrains the evolution scenarios of the Tibetan Plateau. The conclusions are summarized as follows: (1) Tibetan Geoid Ridge is mainly contributed by degree 7 to 10 components in global geoid observation and it is mainly caused by the mantle transition zone density structure. (2) Geoid calculation supports a high-density structure in the mantle transition zone beneath the Tibetan Plateau. (3) This geoid calculation also suggests that the Indian slab subduction scenario is more possible than the lithospheric dripping scenario in the evolution of the Tibetan Plateau.

Acknowledgement

This study was supported by the National Natural Science Foundation of China (92155204). Constructive discussions with Jiashun Hu, Jinshui Huang, and Shijie Zhong are greatly appreciated. Geodynamic computation was supported by the High-performance Computing Platform of Shannon AI.

Open Research

All interpolated seismic tomography data used in this research can be downloaded through Yan et al. (2024). The original seismic tomography data of GYPSUM-S, SEMUCB-WM1 and SL2013sv can be downloaded from Simmons et al. (2010b), French & Romanowicz (2014b) and Schaeffer & Lebedev (2013b), respectively. CitcomS (Moresi et al., 2014) is used for numerical modeling.

General Mapping Tools 6 (GMT6) is used for plotting (Wessel et al., 2019a, b).

Reference:

Adam, C., Yoshida, M., Suetsugu, D., Fukao, Y., & Cadio, C. (2014). Geodynamic modeling of the South Pacific superswell. Physics of the Earth and Planetary Interiors, 229, 24–39.

Chambat, F., Ricard, Y., & Valette, B. (2010). Flattening of the Earth: Further from hydrostaticity than previously estimated. Geophysical Journal International, 183, 727–732.

Chen, M., Niu, F., Liu, Q., Tromp, J., & Zheng, X. (2015). Multiparameter adjoint tomography of the crust and upper mantle beneath East Asia: 1. Model construction and comparisons. Journal of Geophysical Research: Solid Earth, 120(3), 1762-1786. https://doi.org/10.1002/2014JB011638

Chen, M., Niu, F., Tromp, J., Lenardic, A., Lee, C. A., Cao, W., & Ribeiro, J. (2017). Lithospheric foundering and underthrusting imaged beneath Tibet. Nature Communications, 8, 1–10. https://doi.org/10.1038/ncomms15659

Duan, Y., Tian, X., Liang, X., Li, W., Wu, C., Zhou, B., & Iqbal, J. (2017). Subduction of the Indian slab into the mantle transition zone revealed by receiver functions. Tectonophysics, 702, 61-69. https://doi.org/10.1016/j.tecto.2017.02.025

French, S., & Romanowicz, B. A. (2014a). Whole-mantle radially anisotropic shear velocity structure from spectral-element waveform tomography. Geophysical Journal International, 199(3), 1303–1327. https://doi.org/https://doi.org/10.1093/gji/ggu334

French, S., & Romanowicz, B. A. (2014b). SEMUCB-WM1 [Dataset]. UC Berkeley Seismology Lab. https://seismo.berkeley.edu/wiki_br/Broad_plumes_rooted_at_the_base_of_the_mantle_beneath_

major_hotspots

Ghosh, A., Becker, T. W., & Zhong, S. J. (2010). Effects of lateral viscosity variations on the geoid. Geophysical Research Letters, 37, a. L01301. https://doi.org/10.1029/2009GL040426

Ghosh, A., & Pal, D. (2022). Do lower mantle slabs contribute in generating the Indian Ocean geoid low? Tectonophysics, 822, 229176. https://doi.org/10.1016/j.tecto.2021.229176

Ghosh, A., Thyagarajulu, G., & Steinberger, B. (2017). The importance of upper mantle heterogeneity in generating the Indian Ocean geoid low. Geophysical Research Letters, 44(19), 9707–9715. https://doi.org/10.1002/2017gl075392

Hafkenscheid, E., R. Wortel, M. J., & Spakman, W. (2006). Subduction history of the Tethyan region derived from seismic tomography and tectonic reconstructions. Journal of Geophysical Research: Solid Earth, 111(B8). https://doi.org/10.1029/2005JB003791

Hager, B. H. (1984). Subducted slabs and the geoid: Constraints on mantle rheology and flow. Journal of Geophysical Research, 89, 6003–6015.

Hager, B. H. & O'Connell, R. J. (1979). Kinematic models of large-scale flow in the Earth's mantle. Journal of Geophysical Research: Solid Earth, 84(B3), 1031-1048. https://doi.org/10.1029/JB084iB03p01031

Hager, B. H. & O'Connell, R. J. (1981). A simple global model of plate dynamics and mantle convection. Journal of Geophysical Research: Solid Earth, 86(B6), 4843-4867. https://doi.org/10.1029/JB086iB06p04843

Jiménez-Munt, I., & Platt, J. P. (2006). Influence of mantle dynamics on the topographic evolution of the Tibetan plateau: Results from numerical modeling. Tectonics, 25, TC6002. https://doi.org/10.1029/2006TC001963

Li, L., Murphy, M. A., & Gao, R. (2020). Subduction of the Indian plate and the nature of the crust beneath western Tibet: Insights from seismic imaging. Journal of Geophysical Research: Solid Earth, 125, e2020JB019684. https://doi.org/10.1029/2020JB019684

Liu, X., & Zhong, S. (2015). The long-wavelength geoid from three-dimensional spherical models of thermal and thermochemical mantle convection. Journal of Geophysical Research: Solid Earth, 120(6), 4572–4596. https://doi.org/10.1002/2015jb012016

Liu, X., & Zhong, S. (2016). Constraining mantle viscosity structure for a thermochemical mantle using the geoid observation. Geochemistry, Geophysics, Geosystems, 17(3), 895–913. https://doi.org/10.1002/2015gc006161

Mao, W., & Zhong, S. (2019). Controls on global mantle convective structures and their comparison with seismic models. Journal of Geophysical Research: Solid Earth, 124(8), 9345–9372. https://doi.org/10.1029/2019jb017918

Mao, W., & Zhong, S. (2021). Constraints on mantle viscosity from intermediate-wavelength geoid anomalies in mantle convection models with plate motion history. Journal of Geophysical Research: Solid Earth, 126(4). https://doi.org/10.1029/2020JB021561

Moresi, L., Zhong, S., Han, L., Conrad, C., Tan, E., Gurnis, M. et al. (2014). CitcomS v3.3.1 (v3.3.1). Zenodo. https://doi.org/10.5281/zenodo.7271920

Nerlich, R., Colli, L., Ghelichkhan, S., Schuberth, B., & Bunge, H.-P. (2016). Constraining central Neo-Tethys Ocean reconstructions with mantle convection models. Geophysical Research Letters, 43(18), 9595–9603. https://doi.org/10.1002/2016gl070524

Pal, D., & Ghosh, A. (2023). How the Indian Ocean geoid low was formed. Geophysical Research Letters, 50, e2022GL102694. https://doi.org/10.1029/2022GL102694

Parsons, A. J., Hosseini, K., Palin, R. M., & Sigloch, K. (2020). Geological, geophysical and plate kinematic constraints for models of the India-Asia collision and the post-Triassic central Tethys oceans. Earth-Science Reviews, 208, 103084. https://doi.org/10.1016/j.earscirev.2020.103084

Paul, H., & Kumar, M. R. (2022). Strong influence of tomographic models on geoid prediction: Case studies from Indian Ocean and Ross Sea geoids. Tectonophysics, 836, 229429. https://doi.org/10.1016/j.tecto.2022.229429

Ravikumar, M., Singh, B., Pavan Kumar, V., Satyakumar, A. V., Ramesh, D. S., & Tiwari, V. M. (2020). Lithospheric density structure and effective elastic thickness beneath Himalaya and Tibetan plateau: Inference from the integrated analysis of gravity, geoid, and topographic data incorporating seismic constraints. Tectonics, 39, e2020TC006219. https://doi.org/10.1029/2020TC006219

Replumaz, A., Capitanio, F. A., Guillot, S., Negredo, A. M., & Villaseñor, A. (2014). The coupling of Indian subduction and Asian continental tectonics. Gondwana Research, 26(2), 608-626. https://doi.org/10.1016/j.gr.2014.04.003

Replumaz, A., Negredo, A. M., Villaseñor, A., & Guillot, S. (2010). Indian continental subduction and slab break-off during Tertiary collision. Terra Nova, 22(4), 290-296. https://doi.org/10.1111/j.1365-3121.2010.00945.x

Ricard, Y., Fleitout, L. & Froidevaux, C. (1984). Geoid heights and lithospheric stresses for a dynamic Earth. Annales Geophysicae 2, 267–286.

Richards, M. A., & Hager, B. H. (1984). Geoid anomalies in a dynamic Earth. Journal of Geophysical Research: Solid Earth, 89(B7), 5987-6002. https://doi.org/10.1029/JB089iB07p05987

Schaeffer, A. J., & Lebedev, S. (2013a). Global shear speed structure of the upper mantle and transition zone. Geophysical Journal International, 194(1), 417-449. https://doi.org/10.1093/gji/ggt095

Schaeffer, A. J., & Lebedev, S. (2013b). SL2013sv [Dataset]. https://schaeffer.ca/tomography/sl2013sv

Simmons, N. A., Forte, A. M., Boschi, L., & Grand, S. P. (2010a). GyPSuM: A joint tomographic model of mantle density and seismic wave speeds. Journal of Geophysical Research: Solid Earth, 115(B12). https://doi.org/10.1029/2010JB007631

Simmons, N. A., Forte, A. M., Boschi, L., & Grand, S. P. (2010b). GyPSuM [Dataset]. IRIS DMC Data Products. https://doi.org/10.17611/DP/9991624

Spasojevic, S., Gurnis, M., & Sutherland, R. (2010). Mantle upwellings above slab graveyards linked to the global geoid lows. Nature Geoscience, 3(6), 435–438. https://doi.org/10.1038/ngeo855

Steinberger, B., Rathnayake, S., & Kendall, E. (2021). The Indian Ocean Geoid Low at a plume-slab overpass. Tectonophysics, 817, 229037. https://doi.org/10.1016/j.tecto.2021.229037

van der Meer, D. G., van Hinsbergen, D. J. J., & Spakman, W. (2018). Atlas of the underworld: Slab remnants in the mantle, their sinking history, and a new outlook on lower mantle viscosity. Tectonophysics, 723, 309–448. https://doi.org/10.1016/j.tecto.2017.10.004

van der Voo, R., Spakman, W., & Bijwaard, H. (1999). Tethyan subducted slabs under India. Earth and Planetary Science Letters, 171(1), 7-20. https://doi.org/10.1016/S0012-821X(99)00131-4

van Hinsbergen, D. J., Lippert, P. C., Li, S., Huang, W., Advokaat, E. L., & Spakman, W. (2019). Reconstructing Greater India: Paleogeographic, kinematic, and geodynamic perspectives.

Tectonophysics, 760, 69-94. https://doi.org/10.1016/j.tecto.2018.04.006

Wang, Z., Zhao, D., Gao, R., & Hua, Y. (2019). Complex subduction beneath the Tibetan plateau: A slab warping model. Physics of the Earth and Planetary Interiors, 292, 42-54. https://doi.org/10.1016/j.pepi.2019.04.007

Wessel, P., Luis, J. F., Uieda, L., Scharroo, R., Wobbe, F., Smith, W. H. F., & Tian, D. (2019a). The Generic Mapping Tools version 6. Geochemistry, Geophysics, Geosystems, 20, 5556–5564. https://doi.org/10.1029/2019GC008515

Wessel, P., Luis, J. F., Uieda, L., Scharroo, R., Wobbe, F., Smith, W. H. F., & Tian, D. (2019b). The Generic Mapping Tools version 6 [Software]. https://www.generic-mapping-tools.org

Wu, Y., Bao, X., Zhang, B., Xu, Y., & Yang, W. (2022). Seismic evidence for stepwise lithospheric delamination beneath the Tibetan Plateau. Geophysical Research Letters, 49, e2022GL098528. https://doi.org/10.1029/2022GL098528

Xu, M., Huang, Z., Wang, L., Xu, M., Mi, N., & Yu, D. (2020). Lateral variation of the mantle transition zone beneath the Tibetan Plateau: Insight into thermal processes during Indian–Asian collision. Physics of the Earth and Planetary Interiors, 301, 106452. https://doi.org/10.1016/j.pepi.2020.106452

Yan, P., Zhang, N., Liu, X., & Wan, B. (2024) Dataset for Provenance of Tibetan Geoid Ridge and its Implication to the Collision Evolution between India and Tibet [Dataset]. Zenodo. https://doi.org/10.5281/zenodo.10725529

Zhong, S., McNamara, A., Tan, E., Moresi, L., & Gurnis, M. (2008). A benchmark study on mantle convection in a 3-D spherical shell using CitcomS. Geochemistry, Geophysics, Geosystems, 9, a. Q10017. https://doi.org/10.1029/2008GC002048

Figure 1.

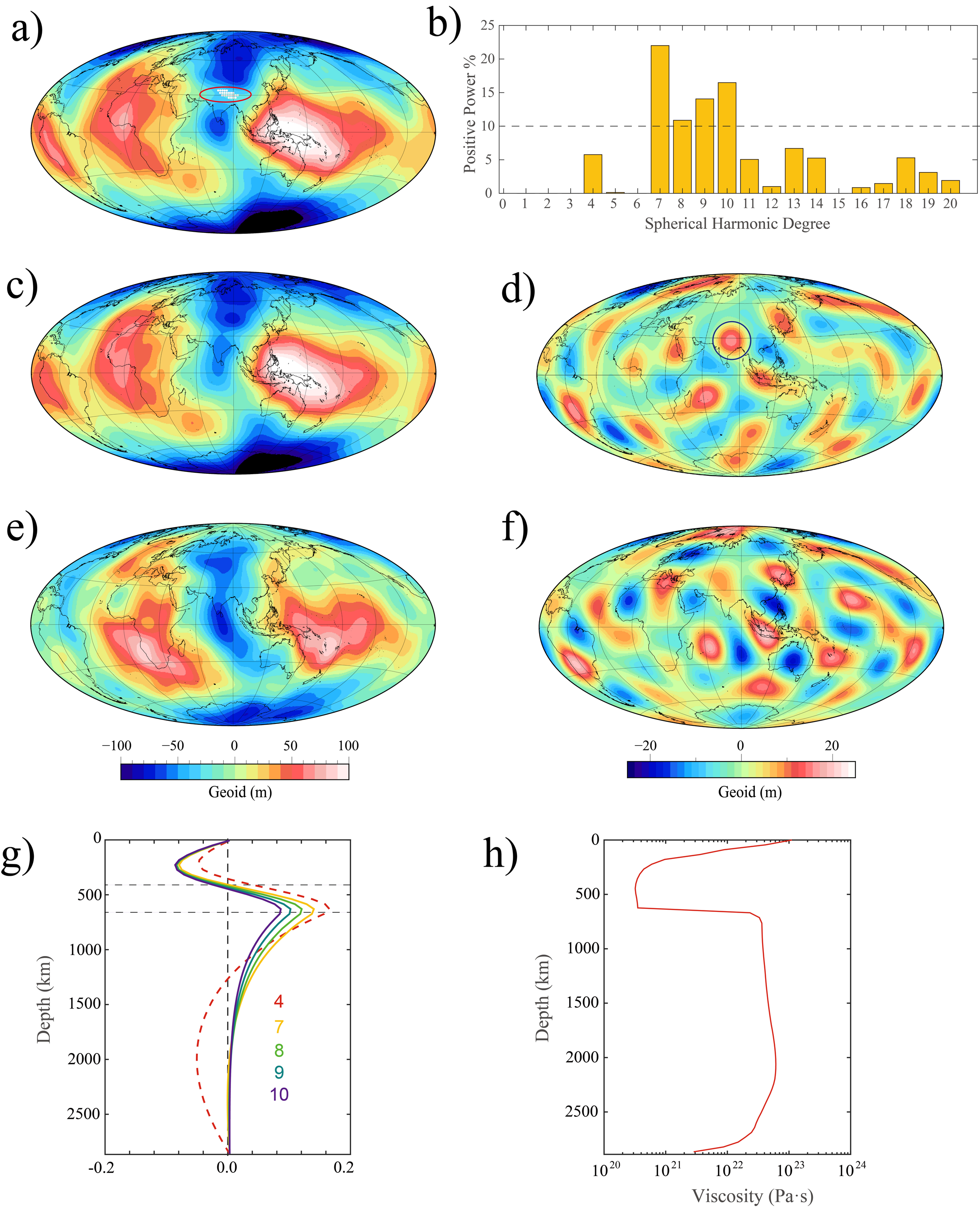
a)
b)
Positive Power %
Spherical Harmonic Degree
c)
d)
e)
f)
−100
−50
0
50
100
Geoid (m)
−20
0
20
Geoid (m)
g)
Depth (km)
4
7
8
9
10
-0.2
0.0
0.2
h)
Depth (km)
Viscosity (Pa·s)

Figure 2.

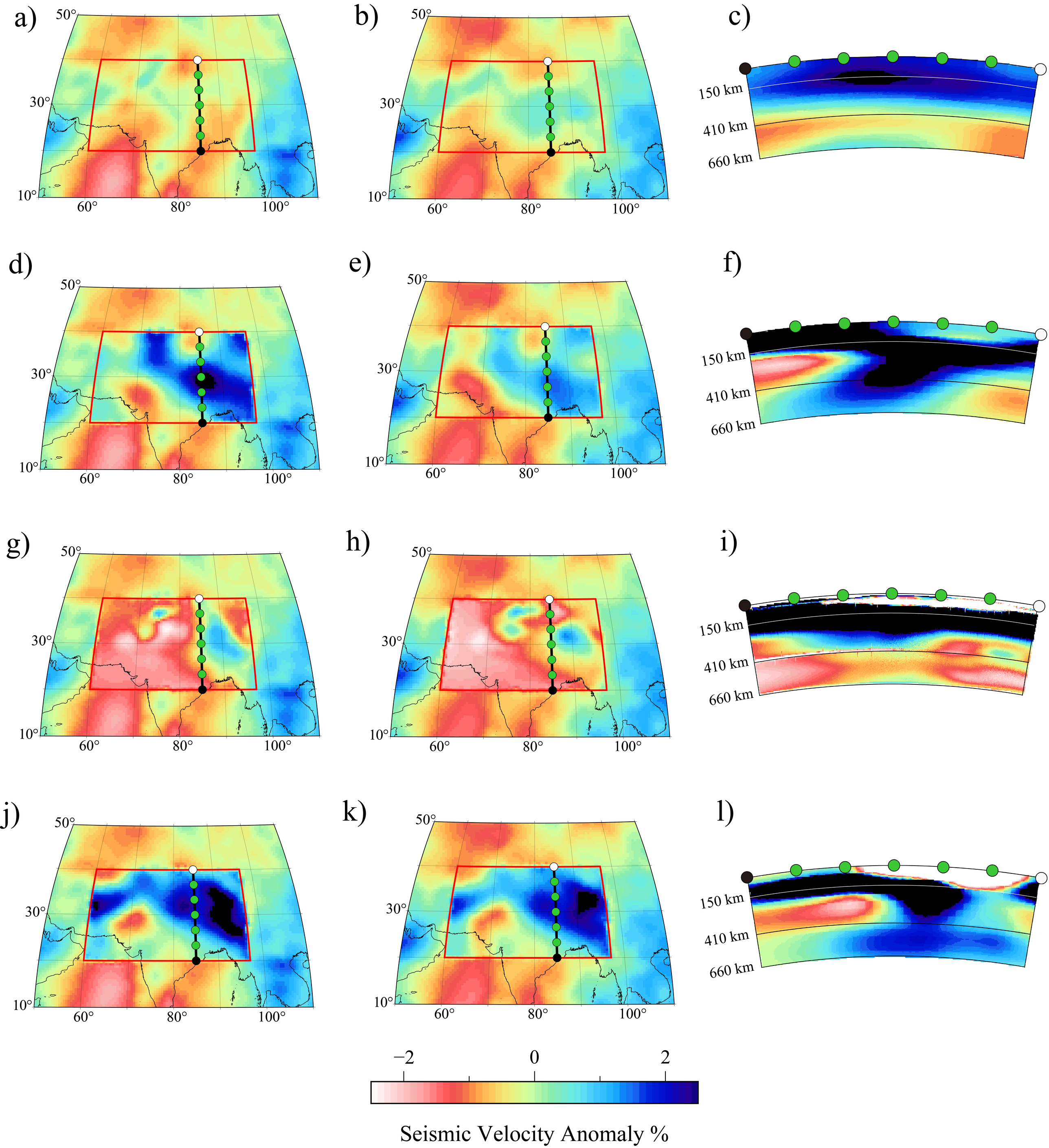
a)
b)
c)
d)
e)
f)
g)
h)
i)
j)
k)
l)
50°
30°
10°
60°
80°
100°
150 km
410 km
660 km
−2
0
2
Seismic Velocity Anomaly %

Figure 3.

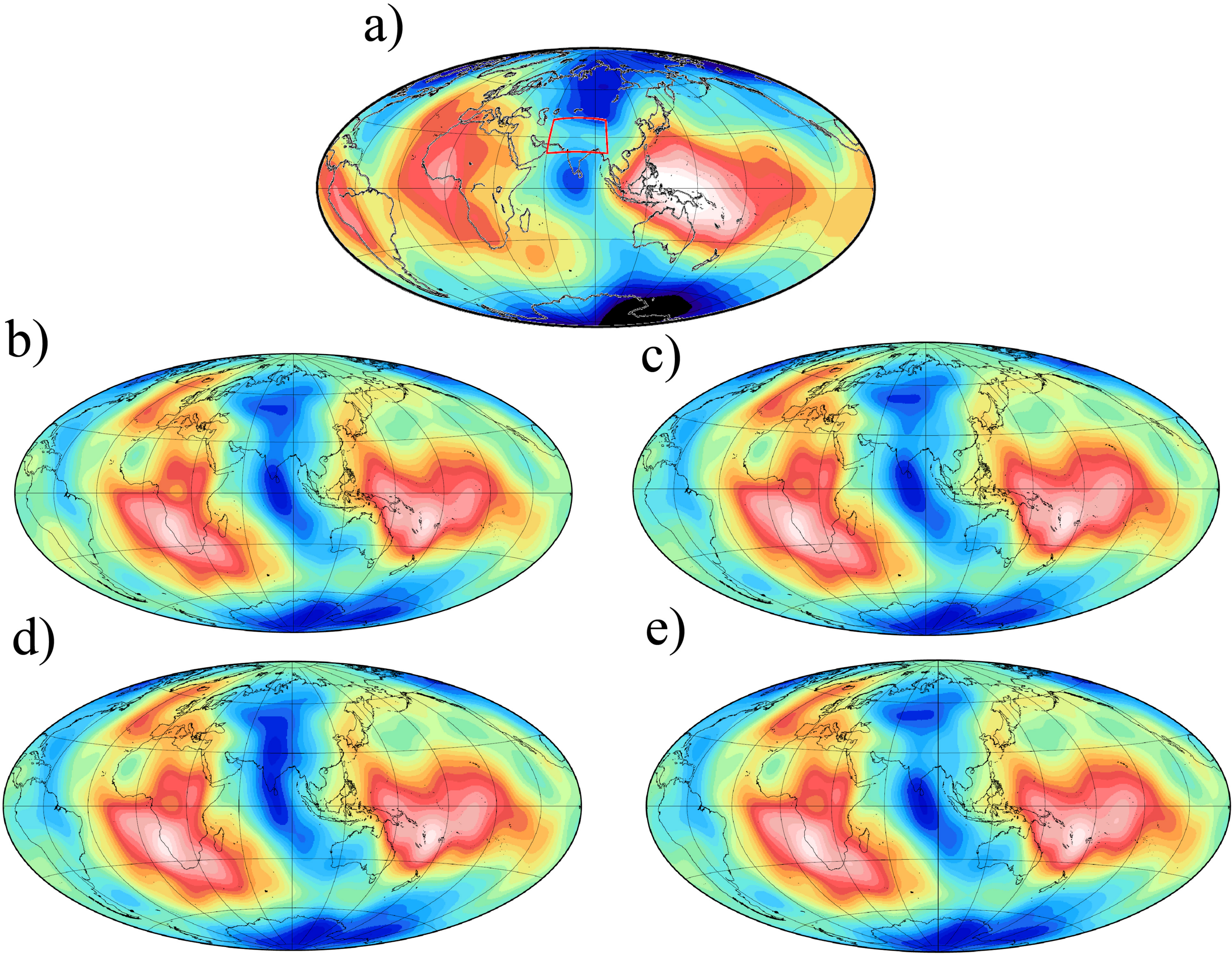
a)
b)
c)
d)
e)
−100
−50
0
50
100
Geoid (m)

Figure 4.

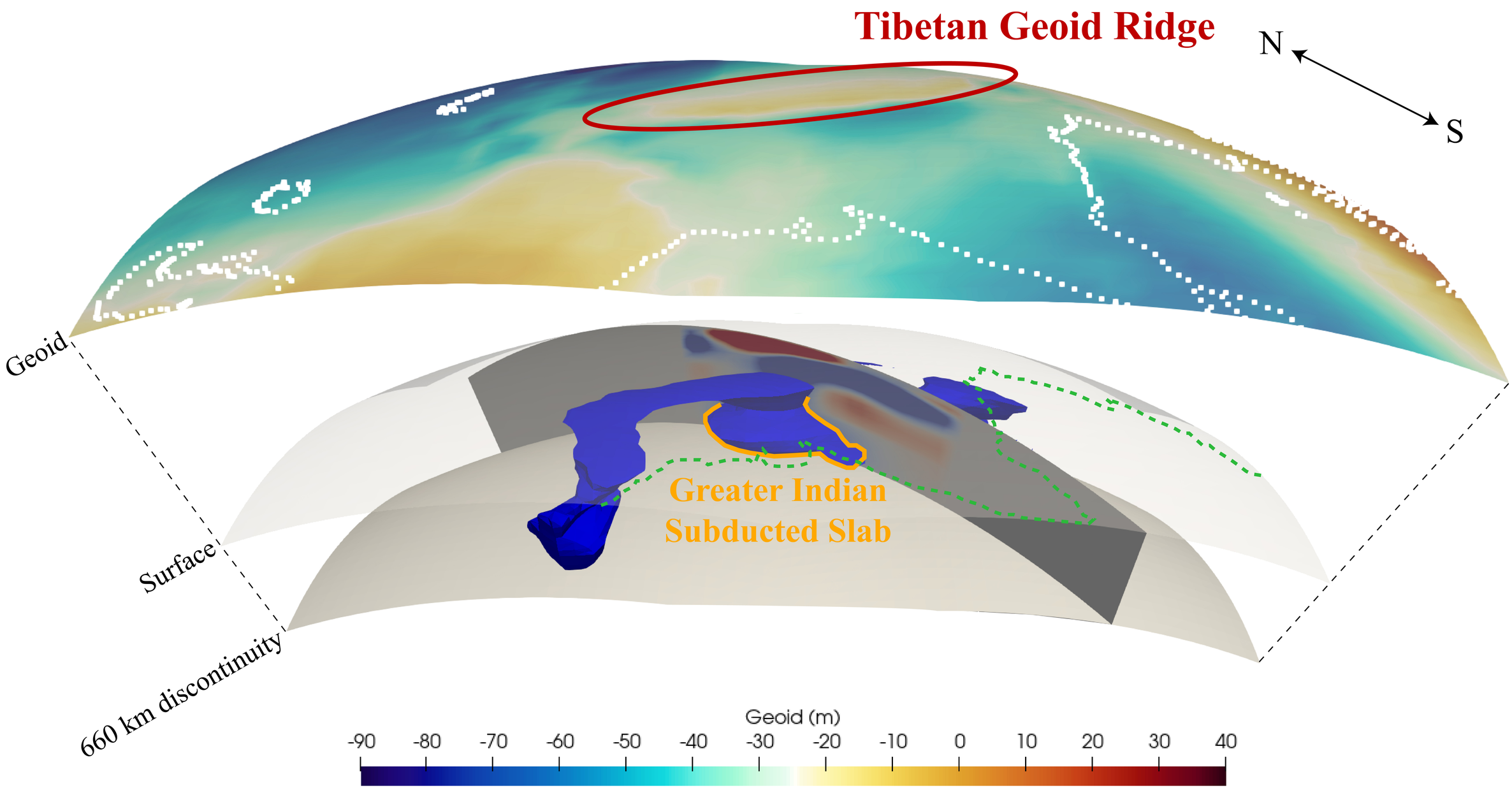
Tibetan Geoid Ridge
N
S
Geoid
Surface
660 km discontinuity
Greater Indian
Subducted Slab
Geoid (m)
-90
-80
-70
-60
-50
-40
-30
-20
-10
0
10
20
30
40